

Enhanced borohydride oxidation on Pd-Ni(OH)₂/C catalyst via hydroxyl enrichment nearby active sites

Jiaqi Zhang^a, Liangyao Xue^a, Wenhui Luo^b, Xing Chen^c, Wenzhe Niu^a, Lin Kang^a, Yexuan Zhang^a, Chenyang Wei^a, Kai Sun^a, Xiao Yang^a, Zhuorong Lu^a, Jianfeng Li^c, Cheng Liu^b, Youyong Li^b, Bo Zhang^{*a}

^aState Key Laboratory of Molecular Engineering of Polymers, Department of Macromolecular Science, Fudan University, Shanghai, 200438, China.

^bInstitute of Functional Nano & Soft Materials (FUNSOM), Jiangsu Key Laboratory for Carbon-Based Functional Materials and Devices, Soochow University, Suzhou, 215123, China.

^cCollege of Energy, College of Chemistry and Chemical Engineering, State Key Laboratory of Physical Chemistry of Solid Surfaces, iChEM, College of Material, Xiamen University, Xiamen, 361005, China.

*Correspondence and requests for materials should be addressed to Bo Zhang (bozhang@fudan.edu.cn) (B.Z.).

Experimental Section

The formation of Pd-Ni(OH)₂/C

During the reaction process, propylene oxide (PO) undergoes hydrolysis, leading to the production of 1,2-propanediol (1,2-PD)¹, which serves as a selective reducing agent due to its limited reducing capacity. Specifically, 1,2-PD reduces Pd²⁺ to Pd⁰, but it is more difficult to reduce Ni²⁺. As a result, the Pd element exists in a metallic state while the Ni element remains in the form of Ni(OH)₂ within the catalyst. The dropwise addition of water and PO contributes to gradual PO hydrolysis and slow Pd²⁺ reduction, which promotes the formation of small metal particles and ensures the uniform dispersion of Pd and Ni(OH)₂ on the carbon support.

Characterization

The morphology of catalysts was obtained by scanning electron microscopy (SEM, Zeiss Ultra 55) with a 3 kV accelerating voltage. High-resolution transmission electron microscopy (HRTEM) images were captured on a JEOL JEM-2100F TEM operated at 200 kV. Scanning transmission electron microscopy (STEM) and energy-dispersive X-ray spectroscopy (EDS) elemental mapping analyses were carried out on a JEOL ARM-200F TEM at an accelerating voltage of 200 kV. X-ray diffraction (XRD) patterns were acquired on Rigaku Smatlab 9 kW X-ray diffractometer instrument using 0.01° divergence with a scan rate of 5° min⁻¹. X-ray photoelectron spectroscopy (XPS) was measured on Thermo Scientific K-Alpha, employing Al K α X-ray radiation (1486.6 eV) for excitation. All XPS spectra data were corrected using C 1s line at 284.8 eV. Ni K-edge X-ray absorption fine structure (XAFS) measurements were carried out at the 1W1B beamline of the Beijing Synchrotron Radiation Facility (BSRF). The samples were prepared by uniformly compressing about 30 mg of catalyst powder into tablets.

In-situ electrochemical surface-enhanced Raman spectroscopy (SERS) measurements

To avoid the interference of carbon powder to the spectral signals, samples used

in the SERS measurements were synthesized without the addition of XC-72. The in-situ SERS measurements were performed using a Renishaw In Via Qontor Raman Microscope with a 785 nm laser. In the measurements, a homemade electrochemical cell, equipped with a Pt wire counter electrode and a Hg/HgO reference electrode, was used. And Ti felts coated by catalyst inks were used as working electrodes. 1 M NaOH and 0.005 M NaBH₄ worked as the electrolyte. The spectra were collected at the steady state under different applied potentials. Each spectrum was integrated for 30 s and averaged by three exposures.

In-situ electrochemical attenuated total reflection Fourier-transform infrared spectroscopy (in-situ ATR-FTIR) measurements

ATR-FTIR measurements were conducted on the Bruker Invenio S FTIR Spectrometer. Catalyst inks were dropped onto a hemicylindrical silicon prism with a gold layer, used as the working electrode. The electrochemical measurements were carried out in a three-electrode system with a graphite rod and a Hg/HgO electrode serving as the counter electrode and the reference electrode, respectively. The electrolyte was 0.1 M NaOH and 0.05 M NaBH₄. Chronoamperometry mode was applied to the system with the potential varying from -1.1 V to 0.4 V vs. Hg/HgO in a stepwise manner. Meanwhile, FTIR spectra were recorded with a time resolution of 16 s per spectrum at a spectral resolution of 4 cm⁻¹.

Electrochemical measurements

All electrochemical measurements were carried out by an electrochemical workstation Metrohm Autolab PGSTAT204. Without specification, the evaluations of electrochemical performance were conducted in a three-electrode configuration at room temperature, in which a glassy carbon coated by the catalyst was the working electrode, and a graphite electrode and a Hg/HgO electrode were used as the counter electrode and the reference electrode, respectively. The electrode potentials mentioned in this paper were rescaled to the reversible hydrogen electrode (RHE) reference by the

following eq. (1).

$$E_{vs. RHE} = E_{vs. Hg/HgO} + 0.098 \text{ V} + 0.059 \times \text{pH} \quad (1)$$

To load the catalyst on the glassy carbon electrodes (GCE, 3 mm in diameter), 2.5 mg catalyst powder was dispersed in 0.5 mL water and ethanol (1:1, v/v) solution, followed by the addition of 40 μL Nafion solution. After sonication, 3 μL of the catalyst ink was dropped onto the GCE. Cyclic voltammetry (CV) measurements at 20 mV s^{-1} were performed in the electrolyte of 1 M NaOH and 0.05 M NaBH₄. Electrochemical impedance spectroscopy (EIS) measurements were carried out in the frequency range of $10^5 \sim 10^{-2}$ Hz with an amplitude of 5 mV in 1M NaOH and 0.05 M NaBH₄. To evaluate the methanol oxidation reaction (MOR) activity of the catalysts, CV measurements at 50 mV s^{-1} were performed for 10 cycles to make the electrodes activated and stabilized before the recording of linear scan voltammetry (LSV) at 5 mV s^{-1} in 1 M NaOH and 1 M CH₃OH.

In this work, the electrochemical active surface area (ECSA) of the catalysts was determined according to Eq. (2)

$$\text{ECSA} = \frac{C_{dl}}{C_s} \quad (2)$$

where C_{dl} is the electrochemical double-layer capacitance of the catalysts, which was measured by CV cycles at various scan rates from 10 mV s^{-1} to 50 mV s^{-1} in 1 M NaOH. The current density was the average of the anode and cathode current densities at the open circuit potential (OCP), which was plotted as a function of the scan rate. The slope of the curve is the C_{dl} value. A general specific capacitance (C_s) of 40 $\mu\text{F cm}^{-2}$ was used to calculate the ECSA.

The electron transfer number (n) during BOR was evaluated by the LSV tests from -0.7 V to 0.2 V vs. Hg/HgO at 10 mV s^{-1} , with different rotating speeds in a solution of 1 M NaOH and 0.01 M NaBH₄. The prepared catalyst ink was dropped onto a glassy carbon rotating disk electrode (RDE, 3 mm in diameter, Tianjin Aida Hengsheng Technology Development Co., Ltd.), which served as the working electrode in a three-electrode system. The rotating speeds of the RDE were 600, 800, 1000, 1200 and 1400 rpm. The n of electrode reaction can be calculated according to the Koutecky-Levich

Eq. (3-4)

$$j^{-1} = j_k^{-1} + j_d^{-1} = j_k^{-1} + B^{-1} \omega^{-0.5} \quad (3)$$

$$B = 0.62nD^{2/3}F\nu^{-1/6}c_0 \quad (4)$$

where j_k is kinetic current density and j_d is diffusion-limited current density, ω (rad s^{-1}) is the rotation speed of RDE, D is the diffusion coefficient of NaBH_4 ($1.6 \times 10^{-5} \text{ cm}^2 \text{ s}^{-1}$), F is the Faraday constant (96485 C mol^{-1}), ν is the dynamic viscosity of the electrolyte ($0.0119 \text{ cm}^2 \text{ s}^{-1}$), c_0 (mol L^{-1}) is the NaBH_4 concentration.

Fuel cell test

In the unit cell of DBFC, Pd-Ni(OH)₂/C, Pd/C and Ni(OH)₂/C were used as the anode, and commercial Pt/C (40%) was used as the cathode. 25 mg anode catalyst was mixed with 2 mL isopropanol, followed by the addition of 180 μL Nafion solution. After ultrasonic dispersion, 200 μL catalyst ink was sprayed onto the Gore select® membrane (M788.12, Sinopharm Chemical Reagent Co., Ltd.) with an active area of 1 cm^2 . The cathode was prepared in the same way on the other side of the membrane. Additionally, carbon paper with a hydrophobic layer served as the cathode GDL, while carbon cloth functioned as the anode GDL. 2 M NaBH_4 in 1 M NaOH solution was employed as the anode fuel with a flow rate of 100 mL min^{-1} . Air was introduced into the cathode at a flow rate of 400 mL min^{-1} with a 100 kPa back pressure. Concerning the stability test, the catalysts were sprayed on the Nafion® 212 membrane, and the measurement was performed in a solution of 1 M NaBH_4 and 2 M NaOH at 60 °C. All other operation conditions remained consistent with those described previously.

DFT calculation method

Density functional theory (DFT) calculations were performed by Vienna Ab-initio Simulation Package (VASP)³, utilizing the projector augmented wave (PAW) potentials with a planewave cutoff energy of 400 eV^{4, 5}. VASPKIT codes were used for post-processing of the VASP calculated data⁶. The exchange-correlation functional⁷ was described by the generalized gradient approximation (GGA) functional of Perdew,

Burke, and Ernzerhof (PBE). The convergence criteria of electronic energies and atomic forces for the calculation of the Pd-Ni(OH)₂ heterogeneous model were 10⁻⁴ eV and 0.05 eV/Å, while the convergence criteria for other calculations were 10⁻⁵ eV and 0.05 eV/Å. A vacuum region of 15 Å was added to all slab models to eliminate the effects between two adjacent layers. The calculated adsorption energy (E_{ads}) was evaluated based on the following equation:

$$\Delta E_{\text{ads}} = E_{\text{sur+adsorbate}} - E_{\text{sur}} - E_{\text{adsorbate}} \quad (5)$$

Where $E_{\text{sur+adsorbate}}$, E_{sur} , and $E_{\text{adsorbate}}$ are the energy for the slab system and the adsorbate, the energy of the slab, and the energy of the adsorbate in a vacuum, respectively. Here, ‘adsorbate’ refers to chemisorbed OH, BH₄⁻.

The free energy change for each step was computed by:

$$\Delta G = \Delta E + \Delta ZPE - \Delta TS \quad (6)$$

Where ΔE is the energy difference between the reactants and the products directly obtained from DFT calculation, ZPE is the zero-point energy, and ΔS is the entropy change. The ZPE and entropic corrections were performed through frequency calculations. The free energy of the proton-electron pair is equal to that of 1/2 H₂(g).

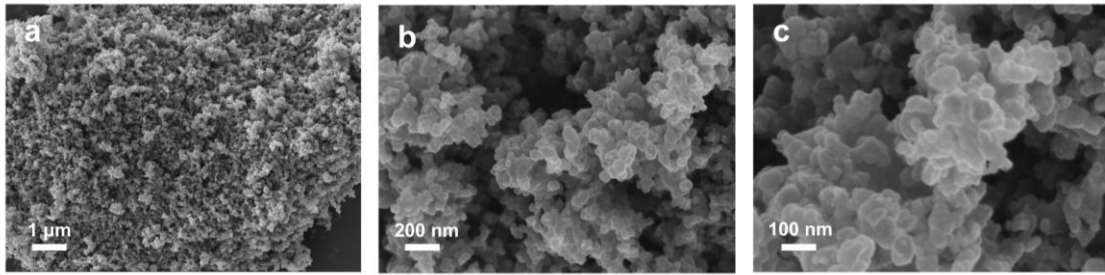


Fig. S1 SEM images of Pd-Ni(OH)₂/C.

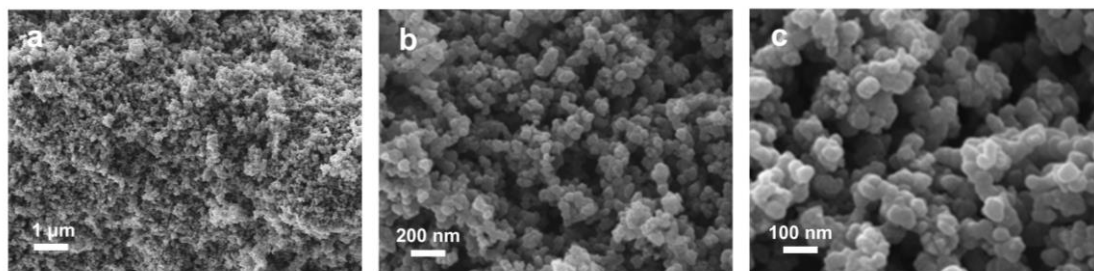


Fig. S2 SEM images of Pd/C.

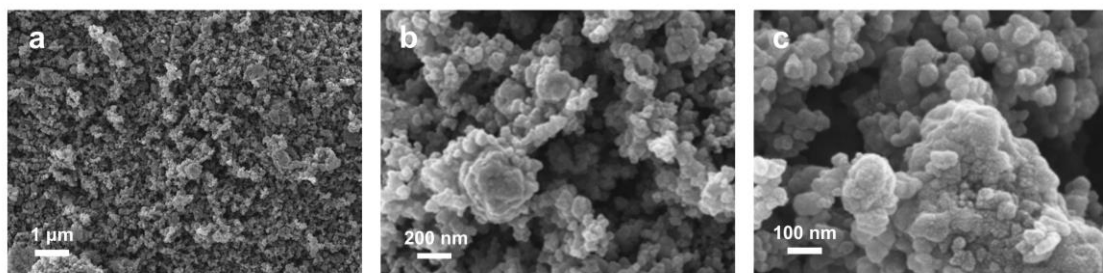


Fig. S3 SEM images of Ni(OH)₂/C.

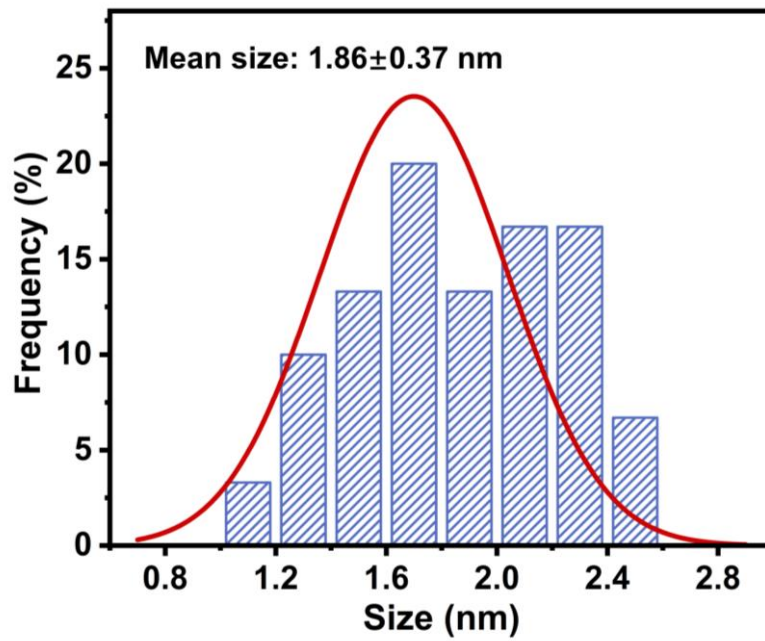


Fig. S4 TEM particle size distributions of Pd-Ni(OH)₂/C.

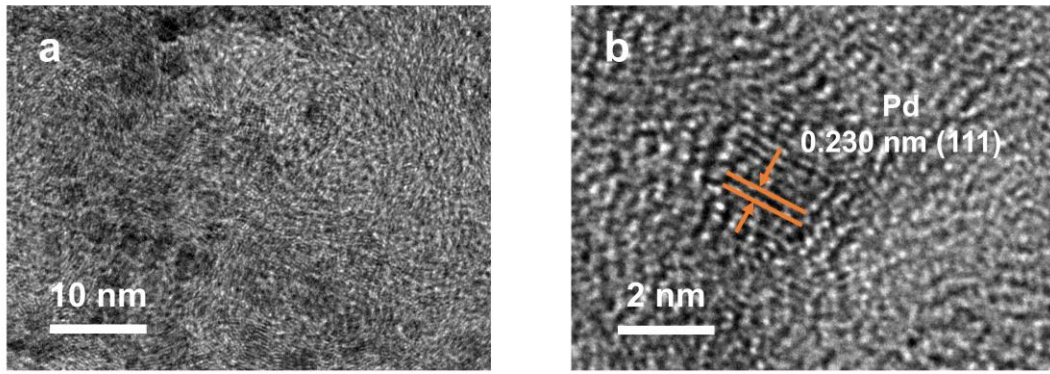


Fig. S5 HRTEM images of Pd-Ni(OH)₂/C.

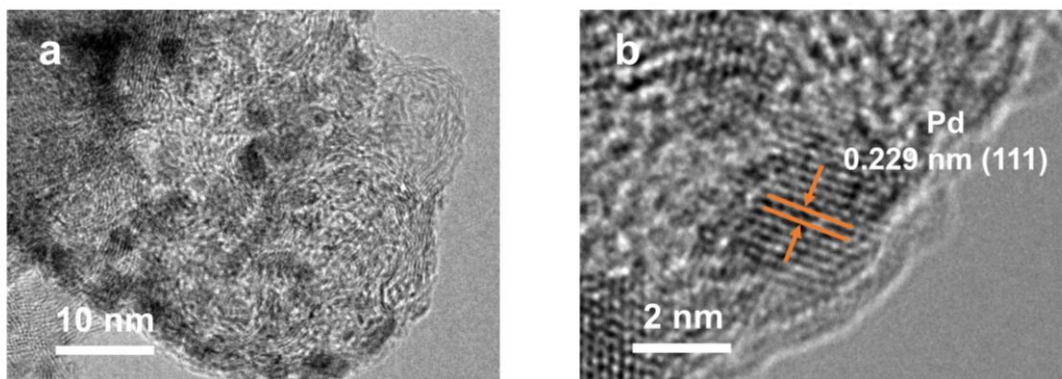


Fig. S6 HRTEM images of Pd/C.

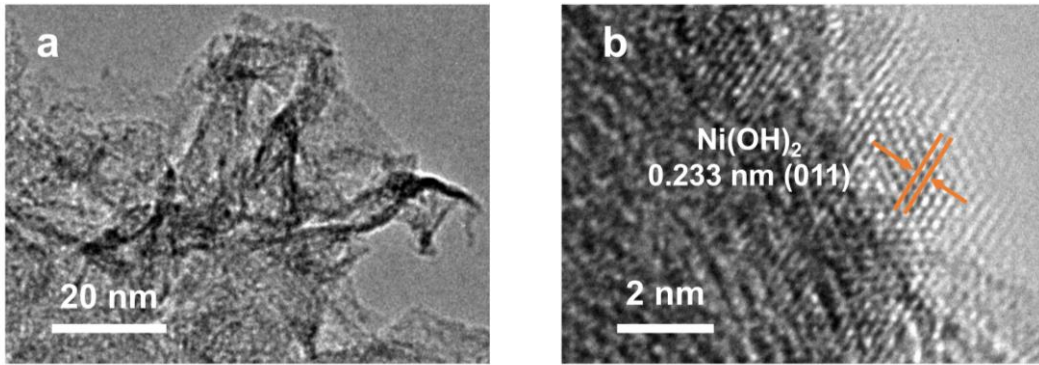


Fig. S7 HRTEM images of Ni(OH)₂/C.

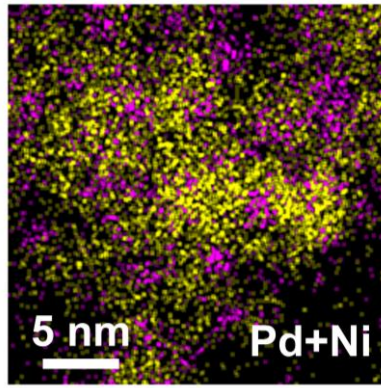


Fig. S8 Overlap of Pd and Ni signals in EDS element mapping for Pd-Ni(OH)₂/C.

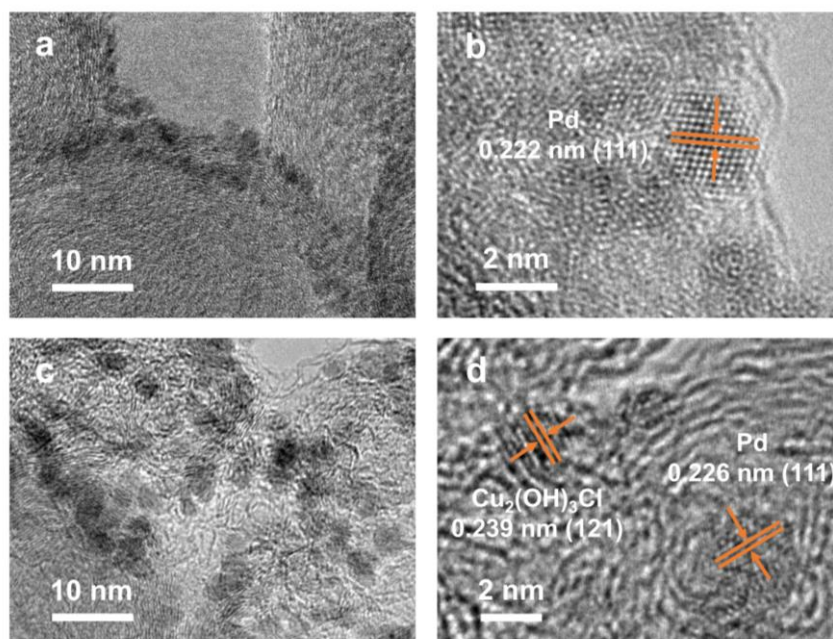


Fig. S9 HRTEM images of (a and b) Pd-Co(OH)₂/C and (c and d) Pd-Cu₂(OH)₃Cl/C.

HRTEM images of the Pd-Co(OH)₂/C and Pd-Cu₂(OH)₃Cl/C catalysts prepared by the same method are presented in Fig. S9. The metal particle sizes on the carbon support are approximately 2-5 nm, indicating that this method is a highly effective strategy for synthesizing catalysts with small and uniform particle sizes.

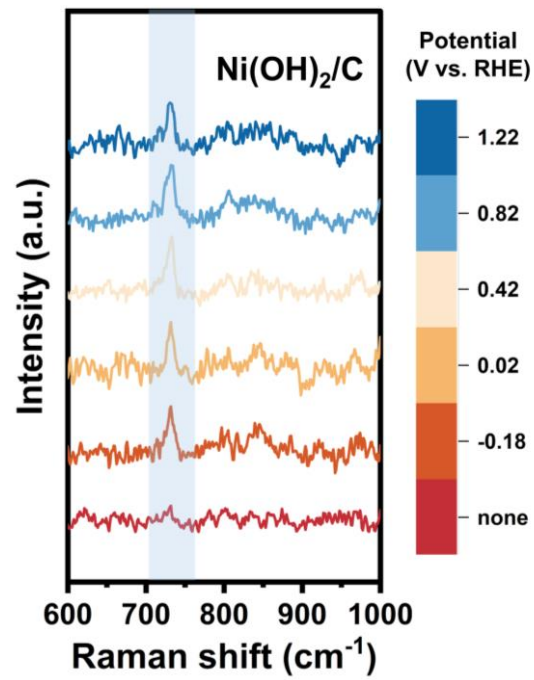


Fig. S10 In-situ electrochemical SERS spectra of Ni(OH)₂/C.

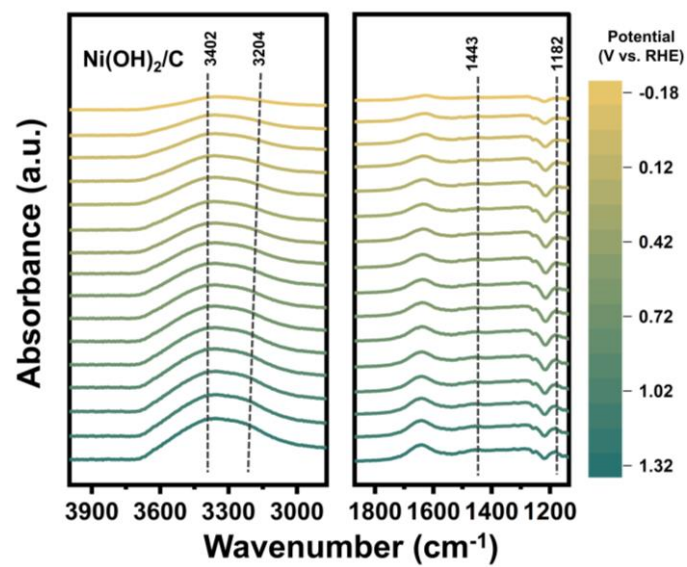


Fig. S11 In-situ electrochemical ATR-FTIR spectra of Ni(OH)₂/C.

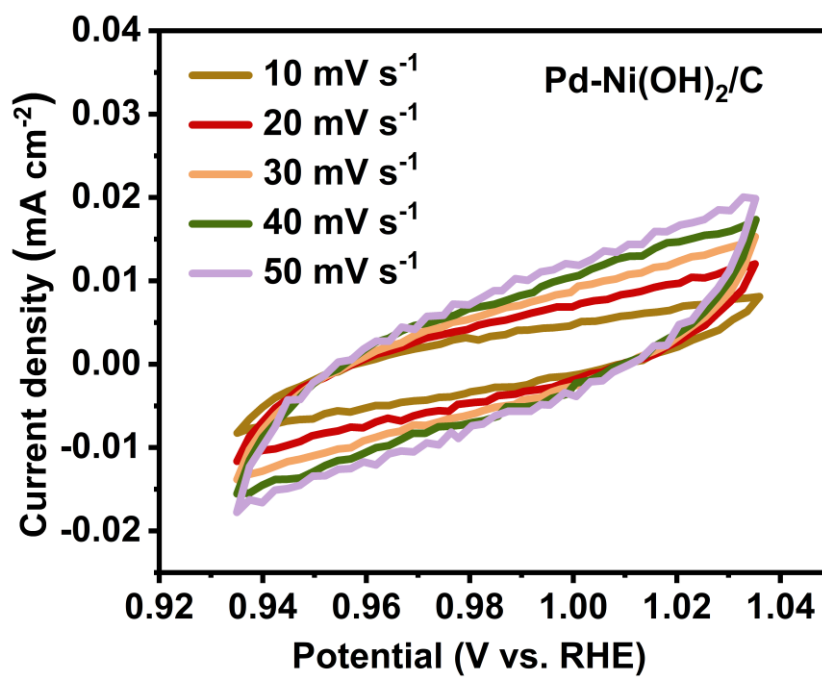


Fig. S12 CV curves collected at different scan rates on Pd-Ni(OH)₂/C in 1 M NaOH.

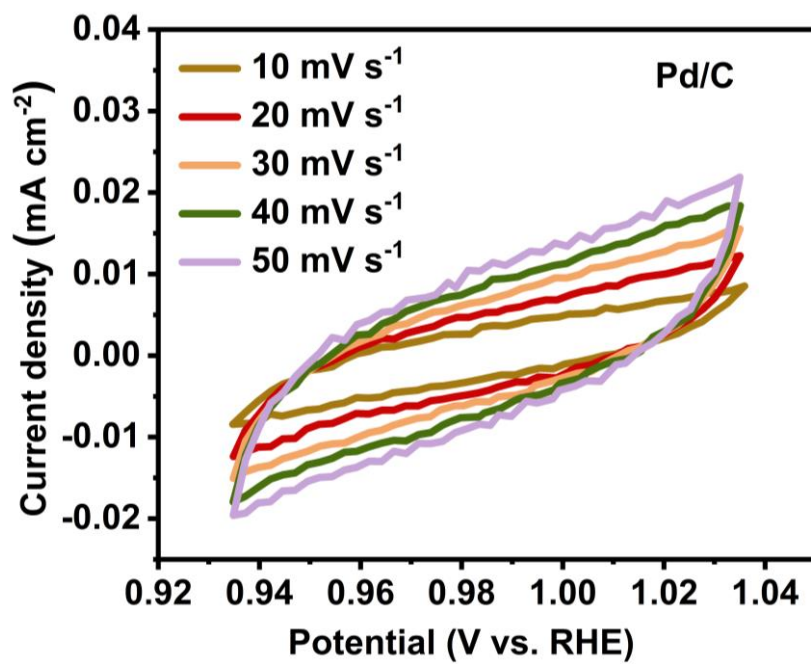


Fig. S13 CV curves collected at different scan rates on Pd/C in 1 M NaOH.

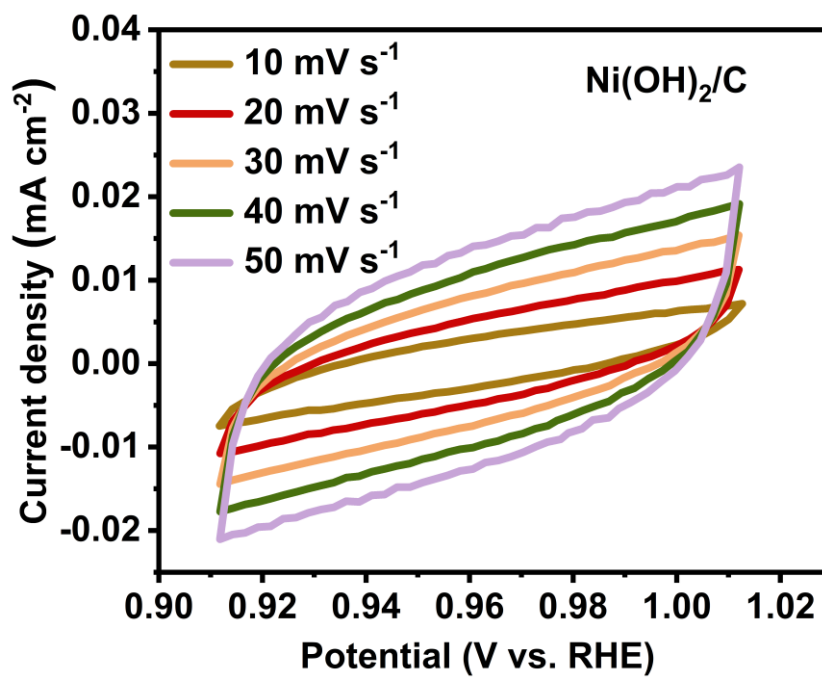


Fig. S14 CV curves collected at different scan rates on Ni(OH)₂/C in 1 M NaOH.

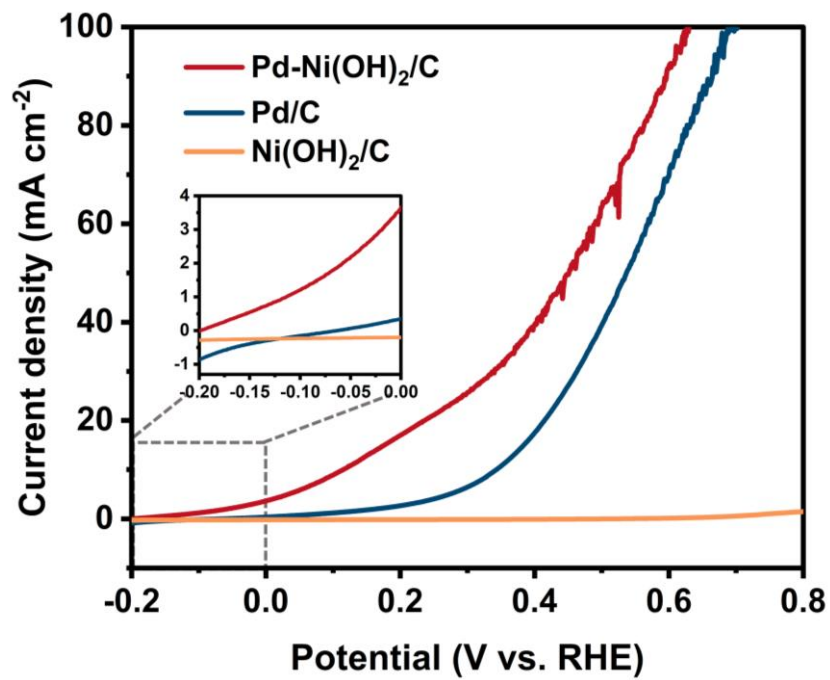


Fig. S15 LSV curves tested on Pd-Ni(OH)₂/C, Pd/C and Ni(OH)₂/C in 1 M NaOH and 0.05 M NaBH₄ at 10 mV s⁻¹.

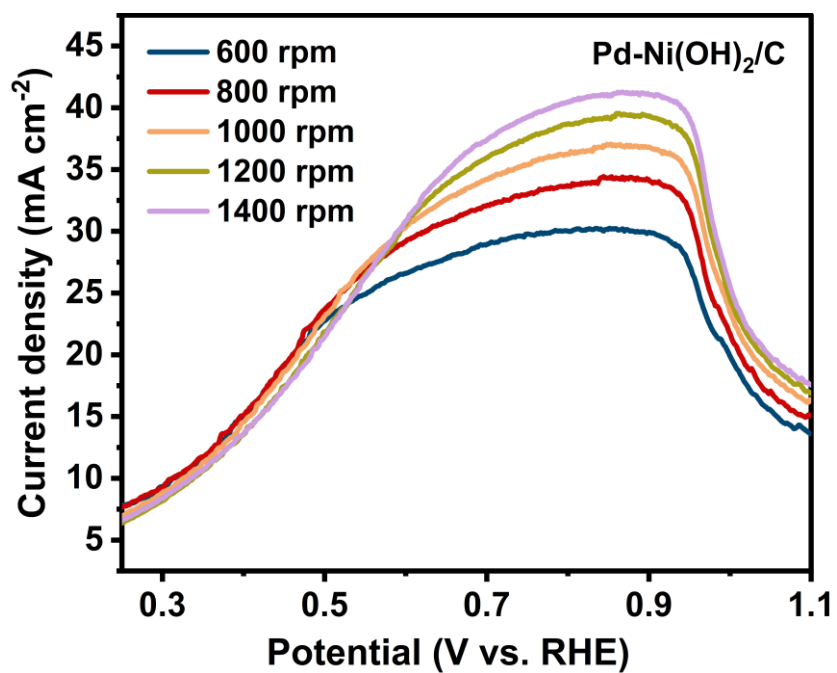


Fig. S16 LSV curves tested on Pd-Ni(OH)₂/C at different rotating rates in 1 M NaOH and 0.01 M NaBH₄ at 10 mV s⁻¹.

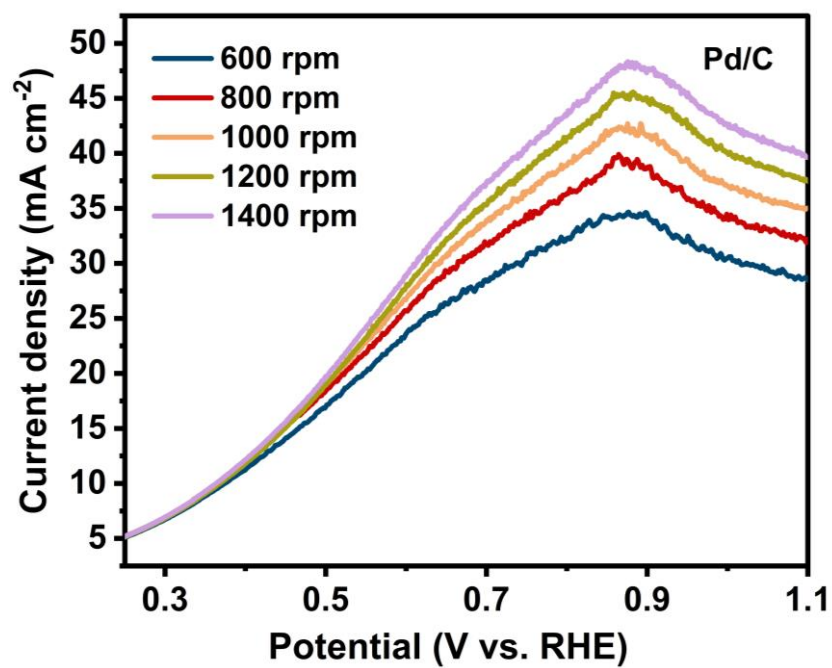


Fig. S17 LSV curves tested on Pd/C at different rotating rates in 1 M NaOH and 0.01 M NaBH₄ at 10 mV s⁻¹.

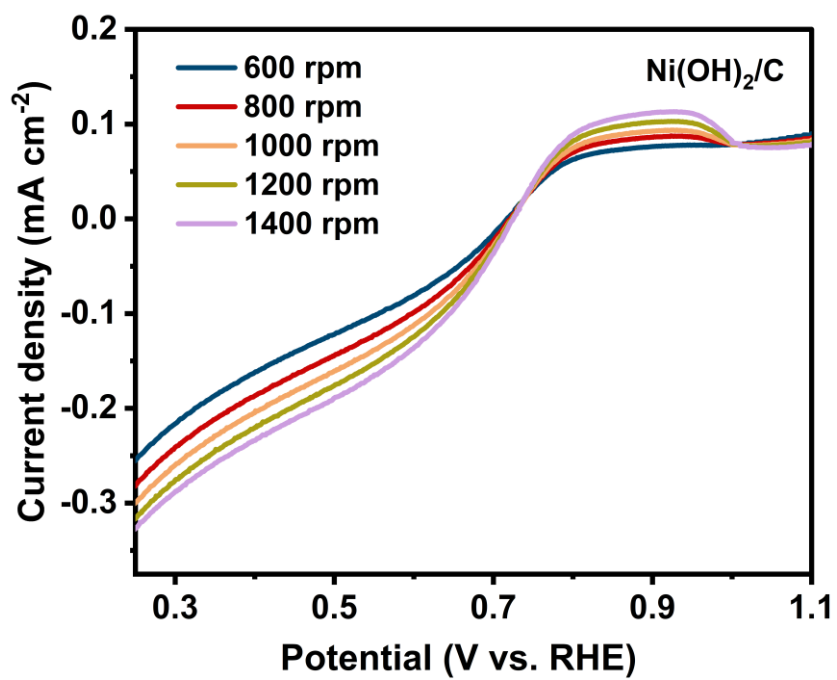


Fig. S18 LSV curves tested on Ni(OH)₂/C at different rotating rates in 1 M NaOH and 0.01 M NaBH₄ at 10 mV s⁻¹.

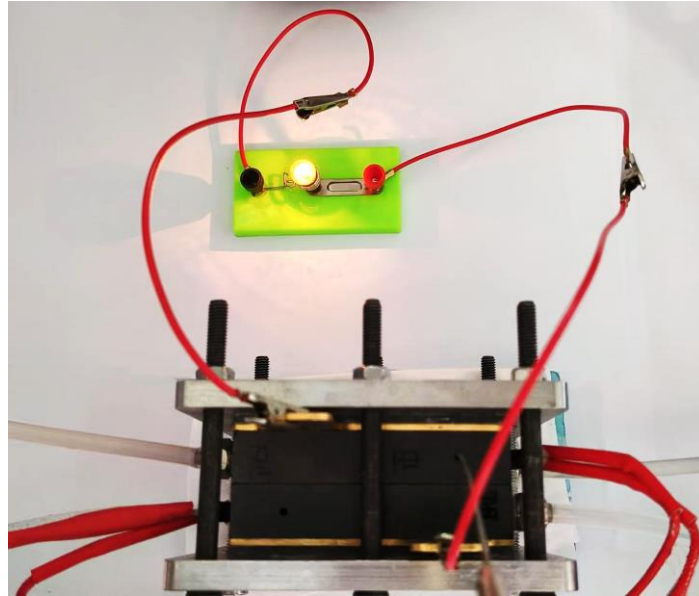


Fig. S19 Demonstration of DBFC with the Pd-Ni(OH)₂/C anode to light up a small bulb.

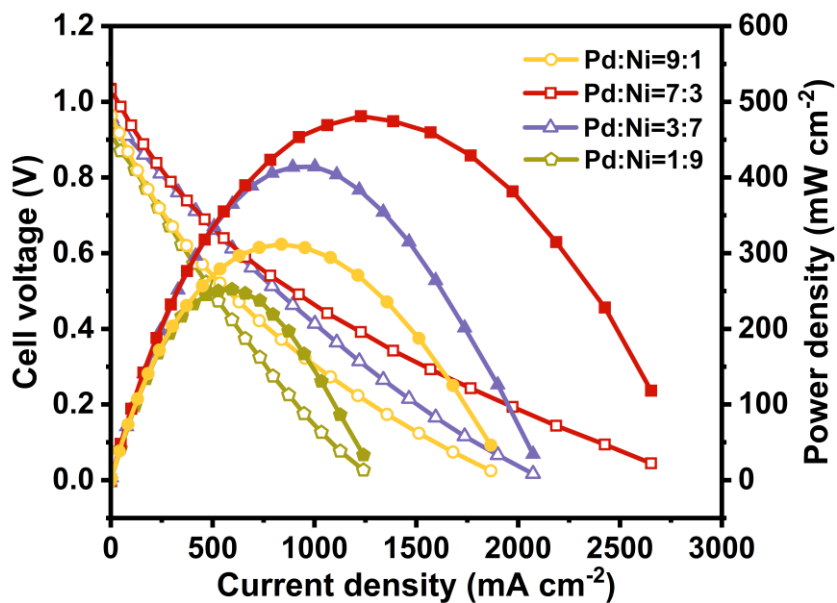


Fig. S20 Comparison of DBFC performance employing catalysts with different mass ratios of Pd to Ni as the anodes.

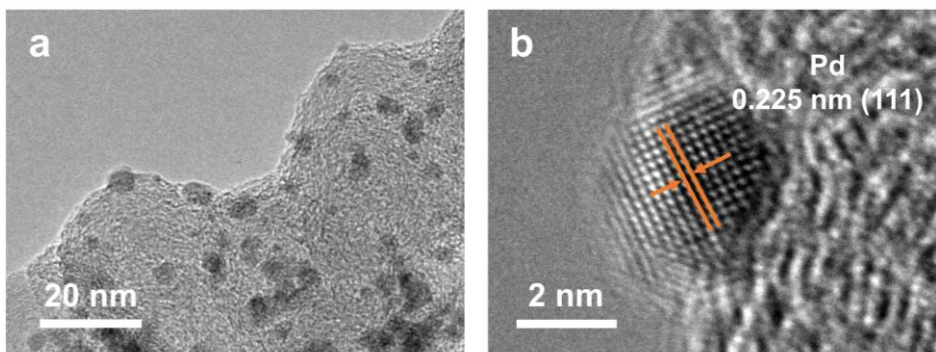


Fig. S21 HRTEM images of Pd-Ni(OH)₂/C after the stability test.

Table S1 Atomic ratios of Pd and Ni in different valence states in Pd-Ni(OH)₂/C, Pd/C and Ni(OH)₂/C.

Sample	Pd²⁺ (%)	Pd⁰ (%)	Pd²⁺/Pd⁰	Ni³⁺ (%)	Ni²⁺ (%)	Ni³⁺/Ni²⁺
Pd-Ni(OH) ₂ /C	48.97	7.97	6.14	17.89	25.16	0.71
Pd/C	72.03	27.97	2.58	/	/	/
Ni(OH) ₂ /C	/	/	/	39.53	60.47	0.65

Table S2 The calculations of ECSA activity and mass activity for Pd-Ni(OH)₂/C, Pd/C and Ni(OH)₂/C at 0.8 V vs. RHE from Fig.4a.

Sample	Current@ 0.8 V (mA)	ECSA (cm²)	Mass (mg)	ECSA activity (mA cm_{cat.}⁻²)	Mass activity (mA mg_{cat.}⁻¹)
Pd-Ni(OH) ₂ /C	2.47	2.95	0.014	0.84	176.43
Pd/C	1.07	3.88	0.014	0.28	76.43
Ni(OH) ₂ /C	0.05	6.53	0.014	0.01	3.57

Table S3 Summary of the peak power density of DBFC using catalysts with different mass ratios of Pd to Ni as the anodes.

Sample	Mass ratios of Pd to Ni	Peak power density (mW cm⁻²)
Pd/C	10:0	268
/	9:1	312
/	7:3	481
Pd-Ni(OH) ₂ /C	5:6	625
/	3:7	414
/	1:9	252
Ni(OH) ₂ /C	0:10	237

Table S4 Comparison of DBFC performances with different anode catalysts and cathodic oxidants.

Anode catalyst	Cathode catalyst	Anolyte	Oxidant	Peak power density (mW cm ⁻²)	Duration (h)	Current density (mA cm ⁻²) @ duration	No.
Au ₄₉ Pd ₅₁ /MW CNTs	Au ₇₄ Ni ₂₆ /MWCNTs	5 wt% NaBH ₄ + 10 wt% NaOH	20 wt% H ₂ O ₂ + 5 wt% H ₃ PO ₄	279.5	1.2	100	1 ⁸
Pd-Ni/N-rGO	Pt/C	1 M NaBH ₄ + 2 M NaOH	2 M H ₂ O ₂ + 0.5 M H ₂ SO ₄	353.84	1	90	2 ⁹
CoP-0.3/CoO _x	Pd	0.4 M NaBH ₄ + 1.5 M NaOH	1.4 M H ₂ O ₂ + 2 M H ₂ SO ₄	277.9	50	100	3 ¹⁰
PtAu/CNT-G	Pt/C	2 M NaBH ₄ + 6 M NaOH	2 M H ₂ O ₂ + 1 M HCl	139	10	135	4 ¹¹
Au-NP@rGO	Pd/C	0.4 M NaBH ₄ + 2 M NaOH	0.8 M H ₂ O ₂ + 2 M H ₂ SO ₄	60	1.5	80	5 ¹²
Ni-np@NC	Pt/C	1 M NaBH ₄ + 3 M NaOH	4 M H ₂ O ₂ + 1.0 M H ₂ SO ₄	218	35	100	6 ¹³
PdNi _{0.3} -B/CNTs	LaNiO ₃	0.8 M KBH ₄ + 6 M KOH	O ₂	127	100	20	7 ¹⁴
Co-Ni-B	LaNiO ₃	0.8 M KBH ₄ + 6 M KOH	O ₂	209	45	80	8 ¹⁵
Pd ₅₀ Cu ₅₀ /C	Pt/C	1 M NaBH ₄ + 6 M NaOH	O ₂	98	60	50	9 ¹⁶
PdNCs/BP	Co(OH) ₂ -PPy-BP	1.52 M NaBH ₄ + 2.87 M NaOH	O ₂	41	50	50	10 ¹⁷
Pd decorated Ni-Co/C	FeCo/C	3% NaBH ₄ + 10% KOH	Air	125.8	2	30	11 ¹⁸
Au@Co-B	LaNi _{0.9} Ru _{0.1} O ₃ /CNT	0.8 M KBH ₄ + 6 M KOH	Air	85	80	20	12 ¹⁹
Pd-Ni(OH)₂/C	Pt/C	2 M NaBH₄+ 1 M NaOH	Air	625	124	200	this work

References

- 1 M. Główka and T. Krawczyk, *ACS Sustain. Chem. Eng.*, 2023, **11**, 7274-7287.
- 2 F. Fiévet, S. Ammar-Merah, R. Brayner, F. Chau, M. Giraud, F. Mammeri, J. Peron, J. Y. Piquemal, L. Sicard and G. Viau, *Chem. Soc. Rev.*, 2018, **47**, 5187-5233.
- 3 G. Kresse and J. Furthmuller, *Phys. Rev. B*, 1996, **54**, 11169-11186.
- 4 P. E. Blochl, *Phys. Rev. B*, 1994, **50**, 17953-17979.
- 5 G. Kresse and D. Joubert, *Phys. Rev. B*, 1999, **59**, 1758-1775.
- 6 V. Wang, N. Xu, J. C. Liu, G. Tang and W. T. Geng, *Comput. Phys. Commun.*, 2021, **267**, 19.
- 7 J. P. Perdew, K. Burke and M. Ernzerhof, *Phys. Rev. Lett.*, 1996, **77**, 3865-3868.
- 8 T. H. Oh, *Renew. Energy*, 2021, **163**, 930-938.
- 9 M. G. Hosseini, V. Daneshvari-Esfahlan, S. Wolf and V. Hacker, *ACS Appl. Energy Mater.*, 2021, **4**, 6025-6039.
- 10 T. Sun, Y. J. Li, Y. Z. Liu, W. Z. Jiao and D. M. Zhang, *Chem. Eng. J.*, 2023, **472**, 10.
- 11 A. Uzundurukan, E. S. Akça, Y. Budak and Y. Devrim, *Renew. Energy*, 2021, **172**, 1351-1364.
- 12 B. P. Li, C. Y. Song, X. M. Huang, K. Ye, K. Cheng, K. Zhu, J. Yan, D. X. Cao and G. L. Wang, *ACS Sustain. Chem. Eng.*, 2019, **7**, 11129-11137.
- 13 B. H. Hu, J. J. Yu, J. Z. Meng, C. L. Xu, J. L. Cai, B. Zhang, Y. P. Liu, D. M. Yu, X. Y. Zhou and C. G. Chen, *ACS Appl. Mater. Interfaces*, 2022, **14**, 3910-3918.
- 14 Y. P. Zhou, S. Li, Y. Z. Chen and Y. N. Liu, *J. Power Sources*, 2017, **351**, 79-85.
- 15 Y. E. Duan, S. Li, Q. Tan, Y. Z. Chen, K. Y. Zou, X. Dai, M. Bayati, B. B. Xu, L. Dala and T. X. T. Liu, *Int. J. Hydrogen Energy*, 2021, **46**, 15471-15481.
- 16 G. Behmenyar and A. N. Akin, *J. Power Sources*, 2014, **249**, 239-246.
- 17 H. Y. Qin, K. J. Chen, C. Zhu, J. B. Liu, J. Wang, Y. He, H. Z. Chi, H. L. Ni and Z. G. Ji, *J. Power Sources*, 2015, **299**, 241-245.
- 18 M. Zhiani and I. Mohammadi, *Fuel*, 2016, **166**, 517-525.
- 19 S. Li, L. N. Wang, J. Chu, H. Y. Zhu, Y. Z. Chen and Y. N. Liu, *Int. J. Hydrogen*

Energy, 2016, **41**, 8583-8588.